Available online at www.sciencedirect.com
ScienceDirect
International Journal of Heat and Fluid Flow 28 (2007) 673–682
International Journal of HEAT AND FLUID FLOW
www.elsevier.com/locate/ijhff

Experimental and numerical investigation of an air pocket immersed and immobilized in a horizontal water duct flow

Assen Vassilev *, Hamda Ben Hadid, Mahmoud El Hajem, Valéry Botton

Laboratoire de Mécanique des Fluides et d'Acoustique, UMR CNRS 5509, ECL/UCBL/INSA-Lyon, France
INSA-Lyon, LMFA, Bât. J. Jacquard, 20 av. A. EINSTEIN, 69621 Villeurbanne Cedex, France

Received 8 November 2006; received in revised form 21 February 2007; accepted 23 February 2007
Available online 6 April 2007

Abstract

In this work, we carry out an experimental and numerical study of a horizontal elongated air bubble (air pocket) immersed in a liquid flow. For this purpose, an air pocket of large aspect ratio is immobilized in a main liquid duct flow. This particular geometry differs from that of previous works since the air pocket is not influenced by the presence of other bubbles (slug/plug flow). The characteristic zones of the air–water interface are identified experimentally and discussed as a function of the Reynolds number up to 26,000. Two-dimensional and unsteady numerical calculations without mass transfer across the air–water interface are carried out in order to study the behaviour of the air pocket under the same conditions as in the experiment. The features of the results are that the shape of the air pocket and its front are quite well reconstructed by the numerical calculations. However, the comparison of the air pocket length evolution with the experimental data shows a slightly different behaviour attributed to the mass transfer across the air–water interface. The numerical study provides a further insight into the wavy behaviour of the interface that is responsible for the vortices in the air pocket.

Keywords: Air pocket shape; Air–water interface; Ripples; Internal secondary flow; Slug/plug flow

1. Introduction

The investigation of elongated gas bubbles or pockets immersed in liquid flows is relevant to many industrial domains: e.g. the development of pipelines and multiphase pumps used in the chemical and petroleum industry (Falcimaigne et al., 2002; Henriot et al., 2002), the air injection in turbomachines in order to diminish the effect of cavitation near the walls (Arndt et al., 1995) or the design of drainage systems (Aimable and Zech, 2003; Minato and Nakajima, 2004). This type of two-phase flows is also encountered in environmental application as described by Benjamin (1968). This author performed a significant work concerning the general form of gas bubbles of large aspect ratio and presented an analytical study relative to the 2D steady gravity currents. He also investigated this configuration through an analogy with the case of an air-filled pocket advancing on the upper side of a confined liquid flow.

Ha-Ngoc (2003) has determined analytically and numerically the flow characteristics and the shape of 2D gas bubbles immersed in a stagnant or flowing liquid. This study considered the surface tension effect in the case when the viscosity does not influence the bubble motion. The analysis of the propagation of the air pocket in a stagnant fluid was found to be in good agreement with the analytical solution of Benjamin (1968) at Bond Number growing up to infinity. Similarly, the comparison with the numerical study of Couët and Strumulo (1987) at small Froude Number (0.2–0.5) exhibited a good agreement.

Renardy et al. (2001) have implemented the Volume-of-Fluid (VOF) method where the interface is modelled applying the piecewise linear construction (PLIC). The paper presents two surface tension models based on the work of Brackbill et al. (1992) that can be implemented in modelling

* Corresponding author. Tel.: +33 4 72 43 70 19; fax: +33 4 72 43 87 18.
E-mail address: assen.vassilev@insa-lyon.fr (A. Vassilev).

0142-727X/$ - see front matter © 2007 Elsevier Inc. All rights reserved.
doi:10.1016/j.ijheatfluidflow.2007.02.005

Nomenclature

D_h	hydraulic diameter of the test duct [m]
$\mathbf{F}_\sigma$	surface tension force [Pa/m]
h	[m] height of the water column under the air pocket (in the test section)
h_{ap}, L_{ap}, w_{ap}	height, length and width of the air pocket [m]
$h_{ap,0}, L_{ap,0}$	initial height and initial length of the air pocket (at $Re = 0$) [m]
$h_{obst}, l_{obst}, w_{obst}$	height, length and width of the obstacle [m]
l_c	capillary length [m]
u_τ	friction velocity [m/s]
U	mean velocity in the x-direction (defined as the ratio between the flow rate and the cross section area) [m/s]
x, y, z	coordinates on the test section [m]
y^+	dimensionless wall parameter [–]

Greek symbols

σ	surface tension (air/water interface) [N/m]
v	kinematic viscosity of water [$m^2\ s^{-1}$]
ρ	density [$kg\ m^{-3}$]

Subscripts and superscripts

ap	air pocket
θ	index associated to an initial parameter
eq	equivalent
*	non-dimensional variable

of moving contact lines. In the first one, the VOF function is extrapolated beyond the flow domain, under condition that its gradient is normal to the interface. At the wall, the normal to the interface is determined by the contact angle. In the second one, the problem is treated as a three-phase configuration using the argument of Young. As this method produces an artificial localized flow, the extrapolated method is considered as a better one.

VOF based direct numerical simulations (DNS) of two types of gas–liquid flow in confined geometries are performed by Wörner et al. (2004). Both flows are modelled in a vertical square mini-channel. This study reveals that the interfacial term is the only source of turbulent kinetic energy.

The accurate reconstruction of the interface remains a problem for the VOF method, when the surface tension effects play an important role and the density ratio of both phases is high. Under these conditions, an artificial velocity field (called "parasitic currents") could appear at the interface and provoke a significant destabilization of the interface. For this reason, the very recent study of Gerlach et al. (2006) compares three existing VOF methods on fixed grids and assesses their capability for the calculation of surface tension-dominant two-phase flows. They are distinguished by the manner how the surface tension force is computed. The first method uses a kernel function for smoothing the interfacial discontinuity. The second one combines two approaches: the VOF and the Level-Set method. The third method includes a parabolic reconstruction of surface tension. A common property of all the analyzed methods is that the interface is represented by piecewise-linear interface segments. This investigation reveals that the third method is more advanced than the other two approaches. The resulting interface is accurately reconstructed and the instabilities due to the parasitic currents are reduced.

In the present work, an air bubble of large aspect ratio is studied experimentally and numerically. It is introduced in a water duct of square cross-section (0.08 m × 0.08 m). Due to the buoyancy, it occupies the upper part of the test section. In order to analyze the behaviour and structure of this isolated air pocket in a water flow, it is immobilized upstream of an obstacle (Fig. 1). Thus, the present study differs from previous works since the air pocket is kept stationary with respect to the test section frame and is not influenced by the presence of other air bubbles or pockets (slug/plug flow). In particular, the geometry of the air pocket and the shape of its interface are investigated here over a wide range of flow rates corresponding to Reynolds number, $Re = UD_h/v$, from 0 to 26,000. Here, U and v denote respectively the mean velocity and the kinematic viscosity of the liquid phase. The hydraulic diameter of the test duct, D_h, is chosen as a constant reference length in accord with the literature concerning slug/plug flows (Fagundes Netto et al., 1999).

This paper is organized as follows: The experimental part of the work is presented in Section 2. Section 3 is dedicated to the numerical study. The comparison between both studies is carried out in Section 4. Finally, Section 5 resumes the results of the actual work.

2. Experimental approach

2.1. Experimental facility

The experimental setup is presented in Fig. 2. This facility is designed in order to produce a gravity driven liquid

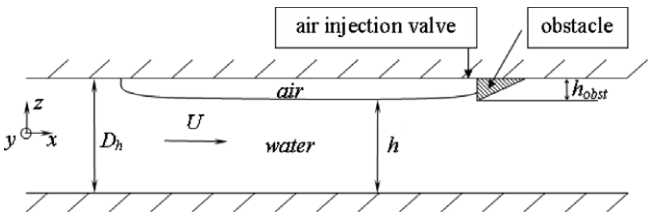

Fig. 1. Sketch of the studied air pocket.

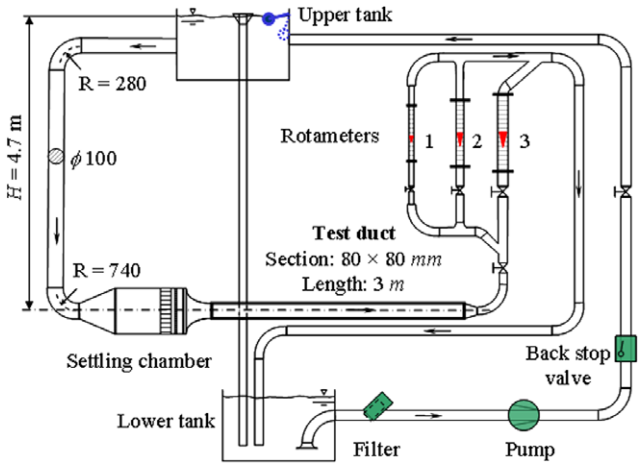

Fig. 2. View of the experimental facility.

flow that circulates between two constant level tanks. The circulating fluid is tap water. The experimental duct of 3 m length has a square section and is entirely made of Plexiglas. An air injection valve is placed in the middle of the test section just upstream of an obstacle fixed at 2.5 m from the entry of the test section (Fig. 1). The obstacle is also made of Plexiglas and its height, length and width are respectively $h_{obst} = 10$ mm, $l_{obst} = 15$ mm and $w_{obst} = 80$ mm. It has a prismatic profile and occupies the whole width and 1/8 of the duct height. Its function is to prevent the air pocket from being carried away by the water flow. A special attention is paid to the external factors acting on the test section: minimization of dilatation and gravity effects by a rigid support, suspension on girths of the test section and the settling chamber connected to the rest of the facility by flexible conducts, isolation from external vibrations by anti-vibration pads and modules.

The air is injected at zero Reynolds number upstream of the obstacle using a medical syringe. Its volume at atmospheric pressure and temperature are known. The initial length, $L_{ap,0}$ is measured under no-flow conditions (at $Re = 0$) from the front of the air pocket to the obstacle. In the following, $L_{ap,0}$ is normalized (Eq. (1)) using the hydraulic diameter, D_h, as a reference length scale:

$$L_0^* = L_{ap,0}/D_h. \quad (1)$$

Three different L_0^* are selected for the experimental study: 8, 14 and 18. They correspond respectively to volumes of 420, 720 and 1020 ml at atmospheric pressure. They are considered much larger than the air water interface capillary length ($l_c \approx 3$ mm). Note that this assumption is also made for the spanwise dimension of the air pocket (80 mm); the numerical approach could be thus reduced to a 2D model. Besides, the horizontal part of the air water interface is long enough to enable the development of undulations.

2.2. Measurement of the air pocket length

The air and water temperatures (T_{air}, T_{water}) and the atmospheric pressure (P_{atm}) are systematically measured and found to be practically constant during each experiment. Before starting the measurements, the water is circulated in order to let its temperature homogenize.

The air pocket remains upstream of the obstacle until the Reynolds number reaches approximately 26,000. For these regimes, no macroscopic air entrainment is noticed even by using optical techniques. Then the mean flow carries away the air bypassing the obstacle. Note that the critical value (Re_{crit}) can vary depending on the initial length, L_0^*, and the way how the flow rate is increased (smoothly or abruptly). Thus, during all the measurements, the Reynolds number is varied very smoothly. The relative uncertainty of the Re values is always smaller than 3.5%.

The downstream extremity of the air pocket is always in contact with the obstacle. The upstream extremity (air pocket front) forms a curved triple contact line with the upper wall (see Fig. 3). In order to take into account this form and to minimize the parallax error, the positions of three points of the contact line are measured: one in the middle and one on each sidewall of the duct. Then, an averaged length is computed from these values assuming a parabolic contact line for small Re ($Re \leqslant 10{,}000$) and linear one for higher Re. The position of each point is determined using a graph paper fixed on the wall of the water duct. The estimated length measurement error is less than 0.4%.

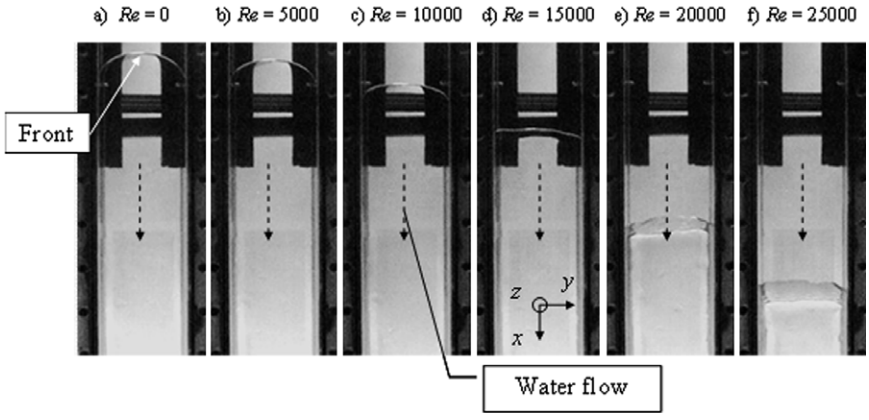

Fig. 3. Evolution of the front of the air pocket as a function of Re (top view).

2.3. Morphology of the interface

2.3.1. Air pocket front

The photographs in Fig. 3 show top views of the air pocket front for Reynolds number varying from 0 to 25,000. It forms triple air–water–Plexiglas contact lines simultaneously with the lateral and upper Plexiglas walls. The water flows from the top to the bottom of the image. In general, as Re grows, the air pocket contracts, i.e. its length diminishes, whereas its height increases very slightly. Thus, the front is displaced in the streamwise direction. At low $Re < 15{,}000$, the contact line in the xy-plane is symmetric and parabolic (Fig. 3a–c). For $Re \geqslant 15{,}000$, the front of the air pocket becomes almost flat. Thus, in order to measure the air pocket length L_{ap} for $Re < 15{,}000$, the front is approximated by a parabolic profile. For higher values of the Reynolds number, $Re \geqslant 15{,}000$, the mean value of L_{ap} is calculated using three points in the y-direction of the air pocket front. At these values of Re, in the vertical direction, the front forms a round and thicker profile as shown in the side-views of Fig. 4d and e. Small capillary waves can be distinguished on the backside of the air pocket front (Fig. 3e and f).

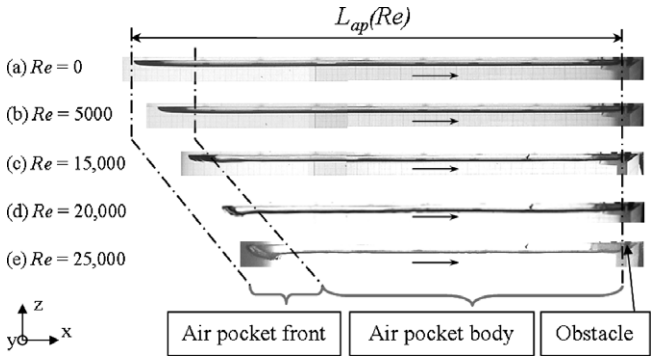

Fig. 4. Evolution of the air pocket length ($L_0^* = 8$) as a function of Re (side view).

2.3.2. Air pocket shape

Generally, the behaviour of the studied air pockets is very similar for all initial lengths ($L_{ap,0}$). Qualitatively, the length L_{ap} diminishes as Re grows as illustrated in Fig. 4.

According to Clift et al. (1978), an air pocket or an air bubble forms under static conditions ($Re = 0$) the so called *Sessile bubble* (Fig. 4a). In this case, the profile is symmetric with respect to the yz-axis passing through the middle of the pocket. When Re grows, the symmetry is broken. In low Reynolds number regimes (till $Re \sim 3000$) the interface remains uniform and no particular zone is distinguished. It is characterized by the presence of *travelling waves* of relatively small amplitude. Beyond this value of Re, a spanwise line arises separating the interface into two regions: the smaller one is located near the obstacle while the second one, much larger, occupies the rest of the pocket. The line appearance could be explained by the inertia-surface tension ratio, i.e. by Weber number defined as $We = \rho U^2 D_h/\sigma$. The increasing Re from 0 to higher regimes leads to the growth of We which reaches unity at $Re = 2828$. The formed *separation line* is present for all higher studied We and Re, i.e. for $We > 1$ and $Re > 2828$. By further increasing Re ($Re \geqslant 16{,}000$), undulations (ripples) arise in the zone upstream of the *separation line* (Fig. 5). These ripples are almost straight. It should be emphasized that they are "frozen" and not standing waves since their highs and lows are fixed in time and space (in the test section frame). Their

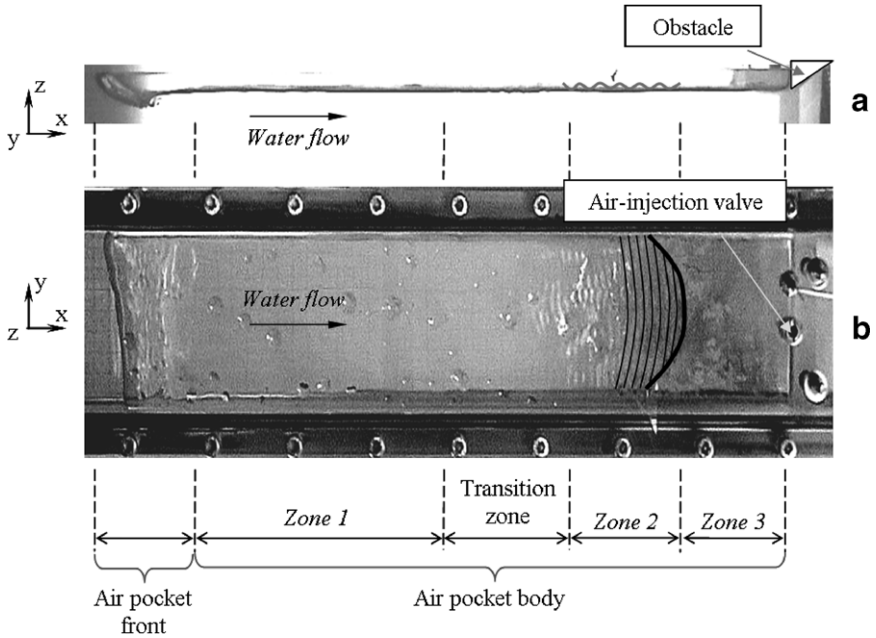

Fig. 5. Global view on the air pocket at $Re = 25{,}000$ ($L_0^* = 8$): (a) side view, (b) top view.

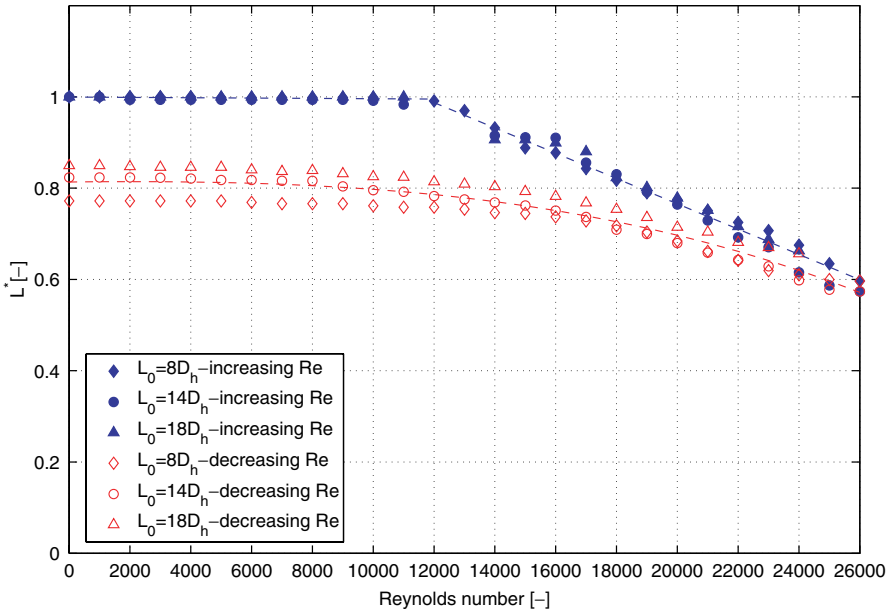

Fig. 6. Evolution of the air pocket length as a function of *Re*.

amplitude grows with *Re*, whereas their wavelength diminishes. The part of the interface where the ripples appear is referred to as *Zone 2*. In the same time, the *travelling waves* continue to occupy the whole *air pocket body* and are overlapped to the "frozen" waves of *Zone 2*.

The interfacial region situated between the *air pocket front* and *Zone 2*, will be named *Zone 1*, whereas the part of the interface located between the obstacle and the separation line will represent *Zone 3*. The frontier between *Zone 1* and *Zone 2* is difficult to distinguish because of the decreasing amplitude of the ripples, in *Zone 2*, from the separation line in the upstream direction. Thus, the separation line is similar to an undular hydraulic jump which appearance is predictable by the Froude number, *Fr*. However, in the considered case, *Fr* based on the mean velocity, *U*, and the water depth in the duct, *h*, remains inferior to the unity on *both* sides of the separation line. This fact excludes the appearance of the hydraulic jump.

Fig. 6 gives the evolution of the normalized air pocket length $L^* = L_{ap}/L_{ap,0}$ as a function of *Re*. Each experiment is performed by progressively increasing the Reynolds number from 0 to 26,000 (except for $L_0^* = 18$, where $Re_{crit} = 24{,}000$ because of the carrying away phenomenon) and then by progressively decreasing *Re* from 26,000 to 0. The duration between two measured points, i.e. between two consecutive Reynolds numbers is 180 s, so the total time of each experiment is exactly the same: 2 h 36 min. The general behaviour of the air pocket length evolution is almost independent of its initial length L_0^*. For $Re \leqslant 12{,}000$, L^* is equal to unity and remains nearly constant. When *Re* is further increased from 12,000 to 26,000, L^* diminishes linearly and reaches 0.56–0.60. With decreasing Reynolds number till $Re = 0$, L^* grows progressively. However, at the end of the experiment, the air pocket length reaches only 0.77–0.85 of its initial length.

Several phenomena could be responsible for this hysteresis-like behaviour in the variation of the air pocket length: air leak, wetting hysteresis and mass transfer between both phases. An additional test excludes the presence of air leak. The air pocket in the case of $L_0^* = 8$ is observed during 24 h at $Re = 0$. No change, neither in its dimensions nor in its position, is detected. Also for *Re* varying from 0 to 26,000 no observable air leak through the duct walls is registered. The effect of the wetting hysteresis is limited. This is confirmed when the flow rate is rapidly increased (till $Re = 26{,}000$) and then immediately decreased to $Re = 0$. The dimensionless length L^* at the end of this experiment is slightly smaller (0.987) than at the beginning of it, but much larger than the observed final length in Fig. 6.

Consequently, the only physical mechanism that can influence the air pocket dimensions is the mass transfer through the air–water interface. It should be reminded that, in the studied range of *Re*, no macroscopic air entrainment is detected neither with the naked eye nor by use of optical techniques (e.g. high-resolution digital camera 12 Megapixels).

3. Numerical approach

The goal of this numerical study is to obtain more insight in the gas pocket behaviour. More precisely, we focus our attention on the structure of the gas–liquid interface and on the shape of the gas pocket front. In order to do that we performed numerical simulation for the same parameters as in the experiment using a commercial code (FLUENT). Because of the similar experimental results obtained for the three gas pockets, only $L_0^* = 8$ is studied numerically using the Volume-of-Fluid (VOF) method in order to reconstruct the interface.

3.1. Description of the numerical model

The two-phase numerical model is 2D and unsteady. The working fluids, air and water, are considered as two immiscible fluids, with constant density and viscosity, separated by an interface. Their physical properties are summarized in Table 1. Note that in the present study the computation is carried out without mass transfer between both phases.

The two-phase flow is described by the conservation equations of mass and momentum. Considering the gas and liquid phases as incompressible Newtonian fluids, they are given respectively by

$$\nabla \cdot \mathbf{v} = 0 \tag{2}$$

$$\frac{\partial}{\partial t}(\rho \mathbf{v}) + \nabla \cdot (\rho \mathbf{v}\mathbf{v}) = -\nabla p + \nabla \cdot [\mu(\nabla \mathbf{v} + (\nabla \mathbf{v})^{\mathrm{T}})] + \rho \mathbf{g} + \mathbf{F}_\sigma. \tag{3}$$

Here $\mathbf{v} = (u, v)$ is the velocity vector, t is the time, p is the pressure, $\mathbf{g} = (0, -g)$ is the gravitational acceleration, $\mathbf{F}_\sigma$ is the surface tension force, ρ and μ are averaged parameters of the density and viscosity that are defined, respectively, by:

$$\rho = \alpha_{\mathrm{L}}\rho_{\mathrm{L}} + (1 - \alpha_{\mathrm{L}})\rho_{\mathrm{G}} \tag{4}$$

$$\mu = \alpha_{\mathrm{L}}\mu_{\mathrm{L}} + (1 - \alpha_{\mathrm{L}})\mu_{\mathrm{G}}, \tag{5}$$

where the index G denotes the gas phase and the index L the liquid phase. In Eqs. (4) and (5), α_{L} is the *volume fraction* of the liquid phase in each computational cell. When the liquid phase occupies entirely the cell, α_{L} is equal to the unity, whereas the volume fraction of the gas is zero. The interface cells contain both phases and are characterized by values of α_{L} between 0 and 1. The model solves the scalar advection equation for the quantity α_{L}:

$$\frac{\partial \alpha_{\mathrm{L}}}{\partial t} + \nabla(\alpha_{\mathrm{L}}\mathbf{v}) = 0. \tag{6}$$

The interface is reconstructed using a piecewise linear scheme (PLIC) which is in agreement with Youngs (1982). This algorithm supposes a linear slope of the phase interface within each cell and considers it by the calculation of the advection of fluid through the cell faces.

The turbulent water flow in the experiment requires an appropriate turbulent model. The RNG k–ε model (*Renormalization Group* k–ε) with enhanced wall treatment has been chosen for this numerical simulation. It is advantageous in regions where the Re is small (near wall regions) and is economic in time and computational resources. More detailed description of this model may be found in the work of Choudhury (1993).

Table 1
Physical properties of water and air

Phase	T [K]	P [bar]	ρ [kg/m^3]	μ [Pa s]	σ [N/m]
Water	288	1.47	998.2	1.0×10^{-3}	0.1
Air	288	1.47	1.8	1.8×10^{-5}	

The segregated, implicit method is used to solve the equations of the problem. The obtained linear system of algebraic equations is solved by means of "point implicit" (Gauss-Seidel) in conjunction with the method AMG (*Algebraic Multigrid Method*).

The jump of the normal stress at the interface is balanced by a surface tension, σ, taken as a constant in this study. The model of surface tension is a continuum surface force model (CSF) suggested by Brackbill et al. (1992). With this model, the addition of surface tension to the VOF calculations results in a source term in the momentum equation. The force acting at the interface is the volume force $\mathbf{F}_\sigma$. In a two-phase system, it can be expressed as:

$$\mathbf{F}_\sigma = \sigma \frac{\rho \kappa \nabla \alpha_{\mathrm{L}}}{0.5(\rho_{\mathrm{L}} + \rho_{\mathrm{G}})}, \tag{7}$$

where κ is the curvature of the interface. It is introduced by the interfacial normal vector $\mathbf{n}$ that is equal to the gradient of the liquid volume fraction α_{L}:

$$\mathbf{n} = \nabla \alpha_{\mathrm{L}}. \tag{8}$$

Thus, the curvature κ is defined in terms of the divergence of the unit normal:

$$\kappa = \nabla \cdot \hat{\mathbf{n}} = \nabla \cdot \frac{\mathbf{n}}{|n|}. \tag{9}$$

Its calculation produces better results when the VOF gradients at the nodes are used rather than the ones computed at the cell centres. Note that the surface tension force is proportional to the averaged density in the cell.

An estimation of the importance of the surface tension force could be obtained from the value of the Weber number. For $Re = 25{,}000$, its maximum values are $We \approx 78$. Thus, the influence of the surface tension could not be neglected. Furthermore, the wall adhesion is taken into account in the model. Note that the conjunction between the surface tension force and the wall adhesion is compatible with the VOF model as described by Brackbill et al. (1992). The contact angle θ_{w} is constant during this study and its value is 90°.

3.2. Geometry and grid mesh

As already mentioned, in the median vertical plane of the test section, the air–water interface is far enough from the side walls. Thus, it is not affected by boundary effects. The 2D geometry and the dimensions of the test section are reproduced in an identical way to those of the experimental facility (Fig. 7). The left extremity corresponds to the inflow and the right extremity to the outflow of the water duct. The prismatic obstacle is situated at 2.5 m from the entry of the test section and its height corresponds to 1/8 of the height of the channel.

The numerical study applies a structured grid with quadrilateral elements. A coarser grid ($G1$) and a finer grid ($G2$) are used in order to adapt the mesh to the studied flow regimes (Table 2). They are sketched respectively in Figs. 8

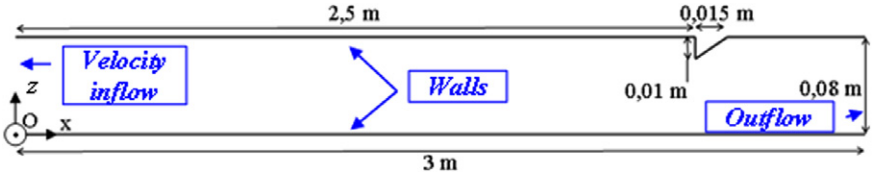

Fig. 7. Sketch of the modelled flow field and its dimensions.

Table 2
Computational parameters applied in the numerical simulation

Grid type	Cells	Re [−]	Δt [ms]	Time steps
$G1$ (coarser)	6.64×10^4	5000, 10,000	1.0	20,000
$G2$ (finer)	1.98×10^5	15,000, 20,000, 25,000	0.5	40,000

and 9. The computational region representing the main interest is the air pocket situated upstream of the obstacle (Region 1). Thus, the grid here is refined and the vertical mesh size is 1/40 and 1/100 for $G1$ and $G2$ respectively. In contrast, the mesh size is relatively coarser in the other regions. The mesh size for $G2$ is everywhere finer than in the case of $G1$. Comparing the number of cells in Table 2, the factor of refinement is close to three. Besides, the computational domain is divided in four regions for $G1$, whereas $G2$ is optimized to the dimensions of the air pocket and contains six regions in order to reduce the computational time. Note also that the mesh fineness in Region 1 verifies that the nearest cell to the wall is situated inside the viscous sublayer. The condition for it is:

$$y^+ = \frac{u_\tau}{\nu}\Delta y < 4, \tag{10}$$

where Δy is the vertical size of the first cell and u_τ is the friction velocity. In our calculation, the wall parameter y^+ is always less than 2. We have also verified that, in the case of $G1$, the coarser grid in the boundary layer of the other computational regions does not influence significantly the modelling results.

For the numerical calculations, the initial pressure is 1.47 bar which corresponds to that measured experimentally at the inside of the duct. At the entry of the duct, the initial turbulent parameters k and ε as well as the velocity profiles for $Re = 5000$ and 10,000 are obtained from preliminary calculations in order to reduce the computational time. They result from the established flow at the exit of the duct, when the air pocket and the obstacle are absent. For higher Re, the water velocity profile is chosen uniform at the entry of the duct. This situation corresponds to the experimental conditions.

4. Comparison between the experimental and the numerical approach

The comparison is based on an air pocket length $L_0^* = 8$. The shape of the air pocket front is presented in Fig. 10 for

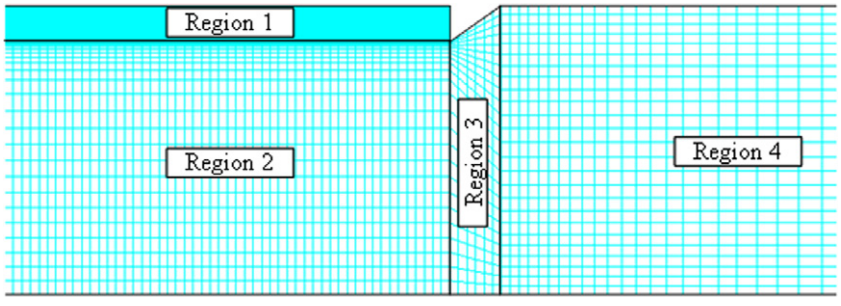

Fig. 8. Schematic of grid $G1$.

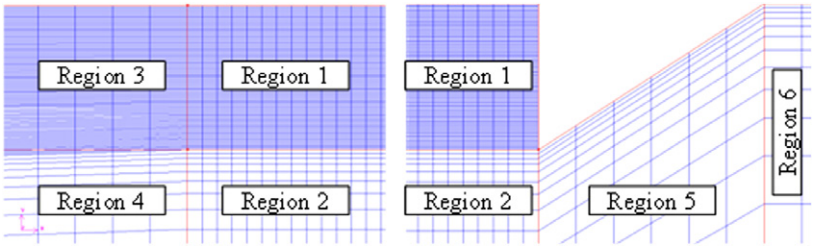

Fig. 9. Schematic of grid $G2$ (zoomed).

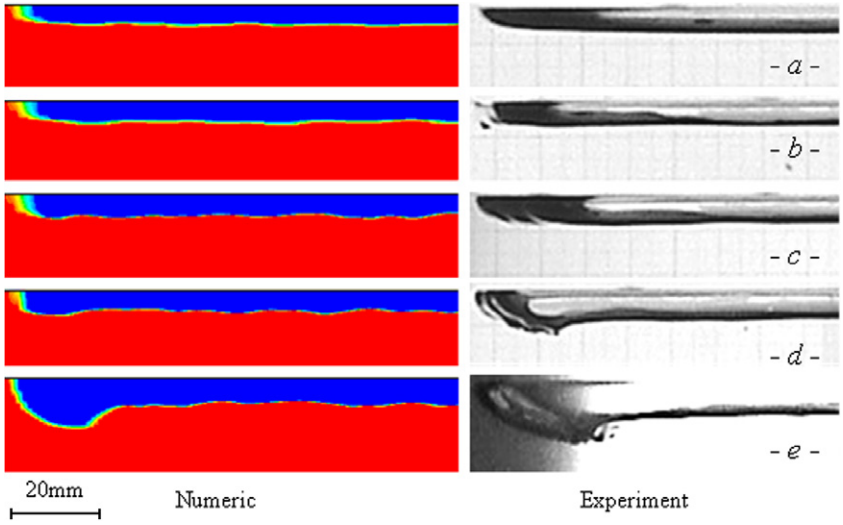

Fig. 10. Comparison between the numerical and experimental studies: (a) $Re = 5000$, (b) $Re = 10{,}000$, (c) $Re = 15{,}000$, (d) $Re = 20{,}000$, (e) $Re = 25{,}000$.

five flow regimes. The numerical results are shown for the time $t = 20$ s. Generally, for $Re \geqslant 15{,}000$, both grids $G1$ and $G2$, show comparable qualitative results about the front shape. However, the numerical result for $G2$ at $Re = 25{,}000$ shows a partial escapement of air due to the mean flow after which the air pocket length is stabilized. As investigated experimentally, $Re = 25{,}000$ is very close to the flow regime at which the carrying away phenomenon could appear. In spite of the air loss, the obtained front shape is comparable to the experimental one.

In Fig. 10, for $Re \leqslant 15{,}000$, the numerical and experimental results show only small modifications in the shape of the air pocket. In contrast, for larger Reynolds number, $Re = 20{,}000$, the numerical result predicts a front that is less influenced by the inertia effects. However, at $Re = 25{,}000$, the shape can be reproduced numerically quite well. The thickening of the front is clearly identifiable and the straight slope downstream the minimum interface level is well reconstructed. The fact that the numerically obtained shape is more compact is probably due to the chosen contact angle of 90°.

As shown in Fig. 11, the length evolution of the air pocket obtained from the numerical computations is compared with the experiment also quantitatively. According to the experimental results shown in this figure, no significant length changes are noted for Re increasing from 0 till 12,000. For this reason, the air pocket length is normalized by the length value obtained for the lowest investigated Reynolds number, namely for $Re = 5000$. This particular length is noted $L_{ap,5000}$. For $Re = 10{,}000$, the air pocket

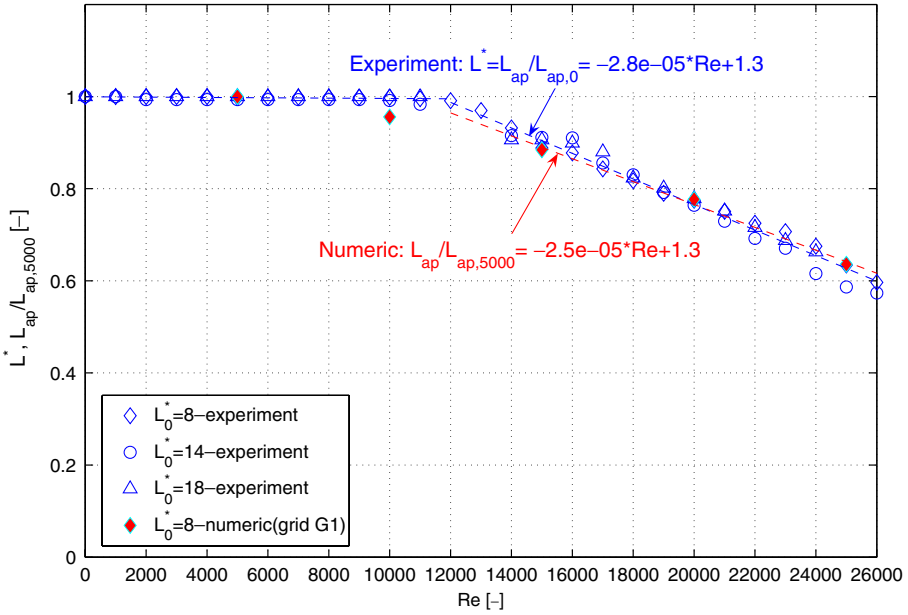

Fig. 11. Quantitative comparison between the numerical and experimental studies of the length evolution slopes.

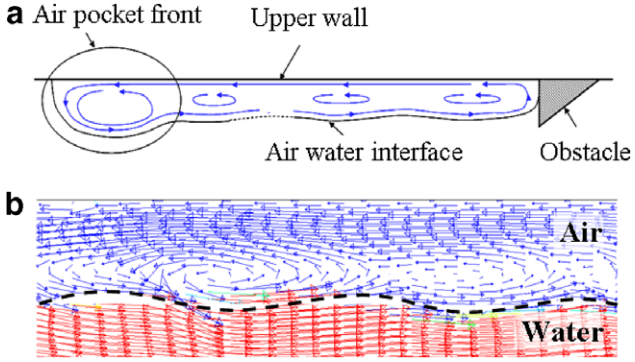

Fig. 12. Recirculation and vortices in the air pocket, secondary vortex in the air pocket at $Re = 25{,}000$ (a) global view (b) computation.

length decrease, obtained numerically, is 3% below those obtained from the experiment. For $Re > 10{,}000$, the agreement between both studies is good and the curves are very close to each other. However, the results from the modelling show a slightly smaller slope. This difference can be explained by the presence of gas dissolution during the experiment, whereas the numerical model is performed without mass transfer.

The recirculation in the air phase presented in Fig. 12 gives a further insight into the behaviour not only of the air pocket but also of the air–water interface. Due to the shear stress, the air in contact with the liquid phase is entrained by it in the downstream direction what produces an air deficit in the front region. At the obstacle, the gas is forced to go up towards the upper boundary and, by continuity, to propagate back towards the air pocket front along the upper wall (Fig. 12a). The two opposite air currents produce an important shear stress within the air pocket. This results in the generation of local secondary vortices oriented in the same direction (Fig. 12b). The vortex centres are situated at the same vertical position as the minima of the interface, whereas the maxima of the interface correspond to the extremities of the vortex. Thus, the characteristic length of the vortices is of the same magnitude as the undulation wavelengths. This is also the case at the air pocket front. Here, in higher regimes ($Re = 25{,}000$), the thickening is accompanied with an increase of the characteristic length of the frontal vortex.

In contrast to the experiment, homogenous undulations from the air pocket front to the obstacle appear on the interface. Thus, in the numerical study, no ripples and no particular zone at the gas–liquid interface are detected.

5. Conclusions

An isolated air pocket of controlled dimensions immersed in a water flow and immobilized by an obstacle is studied experimentally by firstly increasing and then by decreasing Reynolds number. The results show that the air pocket length remains unchanged up to $Re = 12{,}000$. When Re is further increased, the length of the air pocket starts to shrink linearly and reaches 56–60% of its initial length for $Re = 26{,}000$. With decreasing Re till $Re = 0$, the air pocket length grows progressively. However, it reaches at the end of the experiment only 77–85% of its initial length. This hysteresis-like behaviour is attributed to the mass transfer across the air–water interface. Furthermore, the characteristic zones of the air–water interface are identified and discussed in the same range of Reynolds numbers.

The experimental results are completed by two-dimensional, unsteady numerical calculations using a commercial code. The gas–liquid interface reconstruction is based on the Volume-of-Fluid method. The aim of the numerical approach is to provide an access to the velocity field in the gas phase. The obtained air pocket shape and gas–liquid interfacial behaviour are in good agreement with the experiment. The interfacial undulations wavelength is found to be of the same order as the characteristic length of the secondary vortices occurring in the air pocket. Besides, when varying the Reynolds number, the small difference in the air pocket length evolution is attributed to the fact that the modelling is performed without mass transfer through the air–water interface. The numerical modelling can be improved by implementing this phenomenon in a future numerical study.

References

Aimable, R., Zech, Y., 2003. Résultats expérimentaux sur la formation de poches d'air isolées dans un collecteur de drainage urbain. La tribune de l'eau, J. 56 (624), 60–69.

Arndt, R.E.A., Ellis, C.R., Paul, S., 1995. Preliminary investigation of the use of air injection to mitigate cavitation erosion. J. Fluids Eng. 117 (3), 498–504.

Benjamin, B., 1968. Gravity currents and related phenomena. J. Fluid Mech. 31, 209–248.

Brackbill, J.U., Kothe, D.B., Zemach, C., 1992. A continuum method for modeling surface tension. J. Comput. Phys. 100, 335–354.

Choudhury, D., 1993. Introduction to the Renormalization Group Method and Turbulence Modeling. Fluent Inc. Tech. Memorandum TM-107.

Clift, R., Grace, J.R., Weber, M.E., 1978. Bubbles, Drops and Particles. Academic Press, New York.

Couët, B., Strumulo, G.S., 1987. The effects of surface tension and tube inclination on a two-dimensional rising bubble. J. Fluids Mech. 184, 1–14.

Fagundes Netto, J.R., Fabre, J., Peresson, L., 1999. Shape of long bubbles in horizontal slug flow. Int. J. Multiphase Flow 25, 1129–1160.

Falcimaigne, J., Brac, J., Charron, Y., Pagnier, P., Vilagines, R., 2002. Multiphase pumping: Achievements and perspectives. Oil Gas Sci. Technol., Rev. IFP 57 (1), 99–107.

Gerlach, D., Tomar, G., Biswas, G., Durst, F., 2006. Comparison of volume-of-fluid methods for surface tension-dominant two-phase flows. Int. J. Heat Mass Transfer 49, 740–754.

Ha-Ngoc, H., 2003. Etude théorique et numérique du mouvement de poches de gaz en canal et en tube. PhD thesis, Institut National Polytechnique de Toulouse, France.

Henriot, V., Duret, E., Heintzé, E., Courbot, A., 2002. Multiphase production control: Application to slug flow. Oil Gas Sci. Technol., Rev. IFP 57 (1), 87–98.

Minato, A., Nakajima, N., 2004. Simulation of two-phase flow in pumping stations. Congress of advances in the modelling methodologies of two-phase flows 2004, Lyon, France.

Renardy, M., Renardy, Y., Li, J., 2001. Numerical simulation of moving contact line problems using a volume-of-fluid method. J. Comp. Phys. 171, 243–263.

Wörner, M, Ghidersa, B.E., Ilić, M., Cacuci, D.G., 2004. Volume-of-fluid method based numerical simulations of gas–liquid two-phase flow in confined geometries. Congress of advances in the modelling methodologies of two-phase flows 2004, Lyon, France.

Youngs, D.L., 1982. Time-dependent multi-material flow with large fluid distortion. In: Morton, K.W., Baines, M.J. (Eds.), Numerical Methods for Fluid Dynamics. Academic Press.